Hindawi
Complexity
Volume 2020, Article ID 1064016, 13 pages
https://doi.org/10.1155/2020/1064016

Research Article

The Research on Strain-Softening Characteristics and Local Fracture Law of Deep Granite Roadway

Chuang Sun,[1] **Yunhe Ao**,[1] **and Laigui Wang**[2]

[1]*School of Civil Engineering, Liaoning Technical University, Fuxin 123000, Liaoning, China*
[2]*School of Mechanics & Engineering, Liaoning Technical University, Fuxin 123000, Liaoning, China*

Correspondence should be addressed to Chuang Sun; sunchuang@lntu.edu.cn

Received 2 February 2020; Revised 20 May 2020; Accepted 2 June 2020; Published 22 June 2020

Academic Editor: Átila Bueno

Copyright © 2020 Chuang Sun et al. This is an open access article distributed under the Creative Commons Attribution License, which permits unrestricted use, distribution, and reproduction in any medium, provided the original work is properly cited.

The complex mechanical properties of deep surrounding rocks during excavation and unloading have always been a concern in engineering communities. Based on deep roadway engineering, the mechanical properties of granite strain-softening were investigated by laboratory tests. An exponential relationship between granite peak softening modulus and confining pressure was obtained using a nonlinear fitting method. A strain-softening model was developed based on plasticity theory for granite which took into account the nonlinear dilatancy angle and confining pressure. A mathematical model was developed using FLAC^{3D} as platform. By developing a numerical model for a deep roadway, the local fracture characteristics of deep surrounding rocks under strain-softening conditions were evaluated. It has been found that the postpeak failure of granite had a tendency for brittle-ductile transformation. Under high confining pressure conditions, granite exhibited brittle failure characteristics during the postpeak period, and the postpeak softening modulus was decreased with the increase of confining pressure. From FLAC^{3D} numerical calculations, it was found that the numerical models of different mesh densities had basically the same characteristic curves of surrounding rocks, which showed that the local cracking phenomenon had little effect on calculation results when the convergence constraint method was applied for the calculation of the stability of supporting structures and surrounding rocks. It was seen from the numerical simulation analyses of surrounding rock local fracture properties in deep roadways that plastic shear strain appeared in the local areas of roadway vault and arch foot, which basically coincided with the damage location and depth of surrounding roadway rocks.

1. Introduction

Local rupture of rock masses, which refers to successive ruptures and unfractured areas in surrounding rocks on roadway sides and working faces, is common in deep mining [1, 2]. The local rupture phenomena of rock masses decrease the bearing capacity of surrounding rocks. This process is considered as a major reason for the progressive failure of surrounding rocks after the peak excavation process [3]. In actual engineering, brittle failure characteristics are generally observed after the strength of rock reaches its peak value. That is to say, rocks generate and develop cracks under stress and show complex mechanical behaviors such as strength attenuation and expansion in the areas with the maximum strength [4, 5]. Laboratory tests revealed a clear correlation between the mechanical properties of rocks after the peak and confining pressure [6]. In other words, rocks are transformed from brittle failure under low confining pressures to plastic flow failure under high confining pressures. Postpeak brittleness and ductile failure processes could be attributed to the rock strain-softening behavior. In deep rock mining, the strain-softening behavior of rocks can highly affect the local fracture characteristics and stability of surrounding rocks.

Many research works had been conducted on the local fracture of deep rock masses. Ma et al. [7] showed that the creation of zonal disintegrations is mainly dependent on in-suite stress levels and material heterogeneities. The fracture patterns formed during zonal disintegration depend on the size and shape of the tunnel as well as local weakness

distribution in surrounding rocks. Makarov et al. [8] established a novel non-Euclidean mathematical model rock masses under high stress values and developed methods to determine model parameters and major relationships between rock mass strength and cracking zone width. Bi and Zhou [9] developed a GPD method-based constitutive model for the simulation of zonal disintegration in deep rock masses. Varas et al. [10] proposed a theoretical analytical method for strain local rupture and investigated the distribution of local fracture zones by establishing numerical models with different fine levels. Egger [11] comprehensively investigated the strain localization of tunnels and found that the phenomenon of strain localization was common during tunnel excavation and unloading. This phenomenon was found to be related to the lithology and ground stress of surrounding rocks and had a certain distribution regularity. The developed theoretical analytical method was used to explain and analyze strain localization phenomenon, and valuable theoretical results were obtained. Li et al. [12] applied numerical methods to simulate the occurrence and evolution of regional rock failure in deep rocks. In relevant findings of recent years, certain randomness and empiricism are witnessed in the peak and postpeak strength parameters of rock masses and the degradation law of rock mass postpeak strength when calculating local fractures in rock masses, especially when numerical analysis software is applied to simulate the calculations.

Investigation of the rock strain-softening behavior can be performed by three approaches. The first approach is to start with laboratory tests and the analysis of postpeak failure characteristics of rock samples. For example, Perez-Rey. et al. [13] studied the total stress-strain responses of several types of intact rock samples such as sedimentary, metamorphic, and igneous rocks through more than 300 triaxial and uniaxial strength tests. Lu et al. [14] performed routine triaxial compression tests on soft mudstone samples to achieve complete stress-strain relationship curves under different confining pressures and obtained a yield surface model for soft rocks having the two state parameters of generalized cohesion and generalized internal friction angle. Yu et al. [15] evaluated the brittle-extended-plastic transition characteristics of Jinping deep-buried marble peaks after experimental deformation. The second approach was the theoretical analysis. For example, Yu et al. [16] studied a time-dependent deformation mechanism in depth and obtained the viscoelastoplastic deformation using a nonassociated flow rule and the modified Nishihara model. Zareifard [17] proposed a numerical-analytical solution for the ground response curve of a tunnel excavated in an elastoplastic strain-softening rock mass by taking into account the gravitational loading. Alejano et al. [18, 19] developed a postpeak strain-softening model on the basis of the Mohr–Coulomb criterion and Hoek–Brown criterion. Sharan et al. [20] provided an analytical expression for the strain-softening model in the Hoek–Brown elastic-brittle-plastic model during the stress-deformation of surrounding rock masses. In the third approach, numerical calculation methods are proposed for reasonably expressing the strain-softening behavior of rocks based on experimental research and theoretical analyses. For example, Ghorbani and Hasanzadehshooiili [21] studied all influential parameters on strain-softening, including novel and previously studied features, and proposed a complete solution for calculating the GRC of circular tunnels. Wang et al. [22] developed a numerical calculation method for the simulation of the evolution characteristics of parameters during the strain-softening of geotechnical media. Also, the stress-strain curves of geotechnical materials during the evolution of different strength parameters were calculated and analyzed based on the Mohr–Coulomb criterion. Zhang et al. [23] presented a large strain numerical solution of a circular tunnel for the ground reaction curve (GRC) in strain-softening rock masses. Sun et al. [24] investigated the interaction between the surrounding rocks of the chamber and the supporting structures by numerical simulation using a plasticity theory-based rock strain-softening model. The above research results are very valuable in engineering applications. However, developing a postpeak strain-softening model for rocks is very complicated, which limits its wide application in practical engineering. The theoretical calculation was oversimplified, and the calculation results had large errors.

In view of the above problems, in this paper, we have studied the mechanical characteristics of strain-softening of granite samples in deep roadway engineering using laboratory tests. An exponential relationship was found between the peak softening modulus of granite and confining pressure using a nonlinear fitting method. Assuming a constant rock dilatancy angle, a plasticity theory based on the strain-softening model of granite was developed by taking into account the influences of dilatancy angle and confining pressure. A mathematical model was developed using FLAC^{3D} as platform. By developing a numerical model for a deep roadway, the local fracture characteristics of deep surrounding rocks under strain-softening conditions were evaluated. The research results enriched the research system of postpeak mechanical behavior and provided references for practical engineering.

2. Rock Strain Localization and Mechanical Model

2.1. Stress Bifurcation and Localization. In a mathematical point of view, stress bifurcation behavior is due to different combinations of boundary conditions and equilibrium equations. In other words, when the critical value of a parameter is reached, stress bifurcation or strain localization occurs [25]. In compression deformation of rocks, local shear fracture zones are created leading to heterogeneous deformation failure. When surrounding rocks on roadway surface reach a specific unloading level p_i during the excavation and unloading of roadways, immediate stress bifurcation and strain localization take place, as shown in Figure 1.

2.2. Mechanical Model of Rock Strain-Softening. In the plastic strain-softening model for rock materials, plastic potential energy equation and yield criterion are expressed by stress

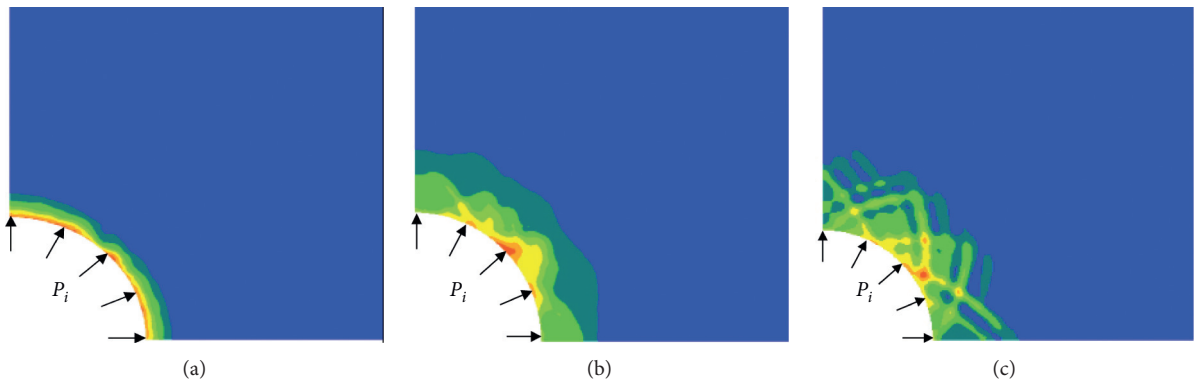

Figure 1: Stress bifurcation and strain localization phenomena. (a) Elastoplastic. (b) Stress bifurcation. (c) Strain localization.

tensor and include softening parameters, as shown in the following equation [26]:

$$f(\sigma_\theta, \sigma_r, \eta) = 0, \tag{1}$$

where $\sigma_\theta$is the maximum principal stress and σ_r is the minimum principal stress.

The Mohr–Coulomb yield criterion could be stated as

$$f(\sigma_\theta, \sigma_r, \eta) = \sigma_\theta - K_\varphi(\eta)\sigma_r - \sigma_c, \tag{2}$$

where σ_c is the uniaxial compressive strength of rock and is defined as

$$\begin{aligned} \sigma_c &= 2c(\eta)\sqrt{K_\varphi(\eta)}, \\ K_\varphi &= \frac{1+\sin-\varphi}{1-\sin-\varphi}. \end{aligned} \tag{3}$$

When it is assumed that c and ϕ in the Mohr–Coulomb constant decay linearly with η, the strain-softening relationship of Mohr–Coulomb could be stated as

$$\omega(\eta) = \begin{cases} \omega^{\mathrm{p}} - \dfrac{\omega^{\mathrm{p}} - \omega^{\mathrm{r}}}{\eta^*}\eta, & 0 < \eta < \eta^*, \\ \omega^{\mathrm{r}}, & \eta \geq \eta^*, \end{cases} \tag{4}$$

where $\omega^p$is the peak parameter, $\omega^r$is the residual parameter, $\eta^*$is the critical softening parameter of rock from strain-softening to residual stage, and ωcan replace the cohesion c and friction angle ϕ in the Mohr–Coulomb model and the constants m and s in the Hoek–Brown criterion. In other words, when $\eta = 0$, rock mass is in elastic deformation stage, when $0 < \eta < \eta^*$, it is in the strain-softening stage, and when $\eta > \eta^*$, it is in the residual stage. The rock softening process is calculated from the postpeak stress-strain curve slope, i.e., the softening modulus M of rock, as shown in Figure 2. When M approaches infinity, elastic and brittle deformation of the material takes place, while when M approaches zero, an ideal elastoplastic deformation is observed. Both cases could be considered as special cases of rock strain-softening behavior.

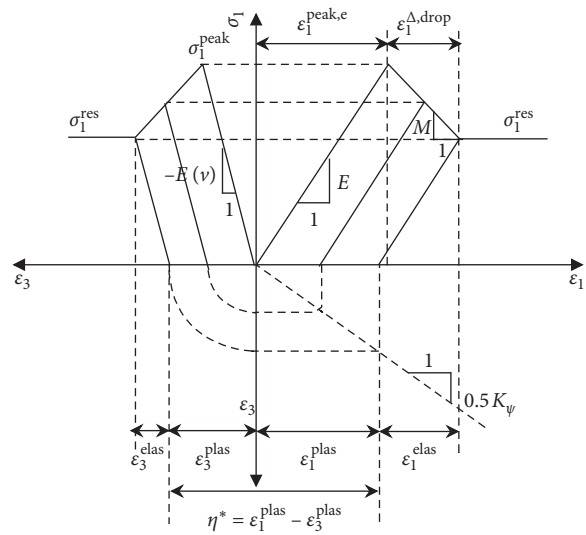

Figure 2: The simplified curve deformation of rock after peak.

Plasticity parameter η^*can be stated in the form of intrinsic variables. In other words, plasticity parameter η^* is defined as plastic shear strain, which is calculated from the difference between the minimum and maximum principal plastic strains. That is

$$\gamma^p = \eta^* = \varepsilon_1^p - \varepsilon_3^p, \tag{5}$$

where $\gamma^p$is the plastic shear strain and $\varepsilon_1^p$and $\varepsilon_3^p$are the maximum and minimum plastic strains, respectively.

Based on the simplified strain-softening curve after the rock peak shown in Figure 2, the maximum principal plastic strain could be stated as

$$\varepsilon_1^p = \varepsilon_1^{\mathrm{peak},e} + \varepsilon_1^{\Delta,\mathrm{drop}} - \varepsilon_1^e, \tag{6}$$

where $\varepsilon_1^{\mathrm{peak},e}$ is the maximum principal strain of elasticity before the peak, $\varepsilon_1^{\mathrm{drop}}$ is the softening strain after the peak, and ε_1^e is the maximum principal strain of elasticity. Under constant confining pressure, the parameters in equation (7) could be stated as

$$\left.\begin{aligned}\varepsilon_1^{\text{peak,e}} &= \frac{\sigma_1^{\text{p}}(\sigma_3)}{E}\\ \varepsilon_1^{\text{drop}} &= \frac{\sigma_1^{\text{p}}(\sigma_3)-\sigma_1^{\text{r}}(\sigma_3)}{-M}\\ \varepsilon_1^{\text{e}} &= \frac{\sigma_1^{\text{r}}(\sigma_3)}{E}\end{aligned}\right\}, \tag{7}$$

where σ_1^{p} and $\sigma_1^{\text{r}}$are peak and residual principal stress, respectively.

Considering dilatancy angle and based on the form of strain increment, dilatancy angle could be expressed as [27]

$$\sin -\psi = \frac{\varepsilon_1^{\text{p}} + 2\varepsilon_3^{\text{p}}}{-\varepsilon_1^{\text{p}} + 2\varepsilon_3^{\text{p}}}, \tag{8}$$

where $\dot{\varepsilon}_j^{\text{p}}(j=1, 3)$ is plastic principal strain rate. equation (8) can be transformed into

$$\dot{\varepsilon}_j^{\text{p}} = -\frac{1}{2}N\psi \cdot \dot{\varepsilon}_j^{\text{p}}, \tag{9}$$

where

$$N_\psi = \frac{1+\sin\psi}{1-\sin\psi}. \tag{10}$$

Under static conditions, the relationship between ε_3^{p} and ε_1^{p} at constant dilatation angle can be calculated from equation (10) as

$$\varepsilon_3^{\text{p}} = -\frac{1}{2}N_\psi \cdot \varepsilon_1^{\text{p}}. \tag{11}$$

Considering the variation of nonlinear dilatancy angle, the dilatancy angle can be calculated using the plastic strain trajectory, as shown in Figure 3. At any point *a*, *b*, and *c* in the plastic strain trajectory, the plastic strain of two discontinuities (*ab* and *bc* intervals) can be expressed as

$$\left.\begin{aligned}\varepsilon_{i,V\_ab}^{P} &= \left(\frac{\varepsilon_{i,V\_a}^{P} + \varepsilon_{i,V\_b}^{P}}{2}\right)\\ \varepsilon_{i,V\_bc}^{P} &= \left(\frac{\varepsilon_{i,V\_b}^{P} + \varepsilon_{i,V\_c}^{P}}{2}\right)\end{aligned}\right\}. \tag{12}$$

where

$$\varepsilon_{V\_ac}^{P} = \varepsilon_{1,V\_ac}^{P} + 2\varepsilon_{3,V\_ac}^{P}. \tag{13}$$

$$\begin{aligned}\varepsilon_{i,V\_ac}^{P} &= \varepsilon_{i,V\_bc}^{P} - \varepsilon_{i,v\_ab}^{P} \quad (i=1,3),\\ \psi &= \arcsin\left(\frac{\varepsilon_{V\_ac}^{P}}{-2\varepsilon_{1\_ac}^{P} + \varepsilon_{V\_ac}^{P}}\right),\end{aligned} \tag{14}$$

Finally, the mathematical relation of constant dilatancy angle and confining pressure η^* could be obtained by combining equations (1) and (6)–(11):

$$\eta^* = \frac{\sigma_1^{\text{p}}(\sigma_3) - \sigma_1^{\text{r}}(\sigma_3)}{E}\,\frac{\xi+1}{\xi}\left(1+\frac{N_\psi}{2}\right). \tag{15}$$

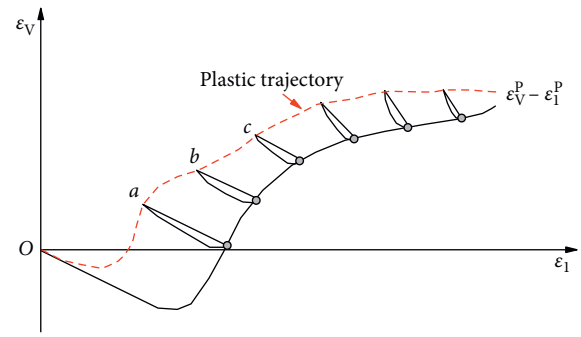

Figure 3: Postpeak plastic strain trajectory of rock.

In FLAC^{3D}, plastic shear strain of the Mohr–Coulomb strain-softening model is expressed by plastic parameter ε^{ps}, and its incremental form is

$$\Delta\varepsilon^{\text{ps}} = \frac{\sqrt{2}}{2}\sqrt{\left(\Delta\varepsilon_1^{\text{ps}} - \Delta\varepsilon_{\text{m}}^{\text{ps}}\right)^2 + \left(\Delta\varepsilon_{\text{m}}^{\text{ps}}\right)^2 + \left(\Delta\varepsilon_3^{\text{ps}} - \Delta\varepsilon_{\text{m}}^{\text{ps}}\right)^2}. \tag{16}$$

where

$$\Delta\varepsilon_{\text{m}}^{\text{ps}} = \left(\frac{\Delta\varepsilon_1^{\text{ps}} + \Delta\varepsilon_3^{\text{ps}}}{3}\right), \tag{17}$$

where $\Delta\varepsilon_j^{\text{ps}}$ $(j=1, 3)$ is the main increment of plastic shear strain.

When considering rock dilatancy behavior, the nonassociated flow law corresponding to plastic shear potential function in FLAC^{3D} could be expressed as

$$g^{\text{s}} = \sigma_1 - \sigma_3 K_\psi. \tag{18}$$

The relationship between plastic parameters and plastic shear strain in FLAC^{3D} is

$$\varepsilon^{\text{ps}} = \frac{\sqrt{3}}{3}\sqrt{1 + N_\psi + N^2{}_\psi}\;\frac{\gamma_{\text{p}}}{1+N_\psi}. \tag{19}$$

3. Experimental Study on Strain-Softening Characteristics of Deep Granite

3.1. Granite Laboratory Test. The granite rock samples selected for experimental tests were collected from the roadway excavation face at a depth of 1,000 meters in Xincheng Gold Mine of Shandong Province in China. Rock blocks had a uniform texture with good overall integrity. Rock blocks were cut into φ 50 mm × 100 mm cylindrical and φ 50 mm × 25 mm disc samples. The processing accuracy of the samples met the requirements of the test specifications recommended by the International Rock Mechanics Society. Brazilian splitting and triaxial compression tests of rocks were conducted on a TAW-2000 microcomputer controlled electrohydraulic servo rigid pressure tester (Chaoyang Instrument Co., Ltd). The test system had the advantages of high accuracy, fast data processing, and high operability and reliability.

In triaxial compression tests, the confining pressure was set at 0 MPa, 2 MPa, 5 MPa, 10 MPa, 15 MPa, and 30 MPa. First, a small hydrostatic pressure was applied to the sample, and then a constant confining pressure was applied. Then, an axial load was applied at a constant strain rate. Axial strain ε_1, radial strain ε_3, axial stress σ_1, and radial stress σ_3 were obtained from the experimental data obtained by the automatic data acquisition system. It was found from repeated experiments on a large number of rock samples that, because of the high homogeneity of granite samples, the dispersions of elastic modulus and peak strength of the rocks were low. The complete stress-strain curves were experimentally obtained for granite samples from typical triaxial compression, as shown in Figure 4(a).

In the Brazilian splitting test, a splitting fixture was placed in the middle of the upper and lower pressure plates of the testing machine. Once the test was started, the clamping screws on both sides of the fixture were loosened and a uniform load at a loading speed of 0.5 MPa/s was applied until failure. Tensile strength ε^{ps} was obtained using the automatic data acquisition system.

It was seen from Figure 4(a) that the rock samples showed elastic and brittle failure during uniaxial compression and were dropped rapidly after reaching peak strength σ_1^{peak}. The residual strength σ_1^{res} of rock samples was about 0 MPa, and they were broken, as shown in Figure 5(a). The failure of rock samples under low confining pressure ($\sigma_3 = 2, 5$ MPa) still showed elastic and brittle failure characteristics. By further increase of confining pressure, the stress-strain curve slope after rock peak was gradually decreased. As the confining pressure was increased, the failure characteristics of rocks tended to change from brittleness to ductility, and the rock failure mode was mainly shear failure after the peak. Based on the peak strength curves of rocks under different confining pressures, it was found that confining pressure also affected the elastic parameters of rocks. In this paper, we have focused on the postpeak mechanical characteristics and connected the peak strength point to the residual strength point. The slope of this line can be defined as the softening modulus of the rock sample, which is denoted by M in this paper, as shown in Figure 4(b). Softening modulus M could be obtained from elastic modulus E as

$$M = -\xi \cdot E. \tag{20}$$

The peak elastic parameters of rock were simply calculated, and the values of elastic modulus $E = 34.4$ GPa and Poisson's ratio $\nu = 0.28$ were obtained.

Characteristics of typical rock destruction are shown in Figure 5.

3.2. Study on the Peak and Postpeak Strength Characteristics of Granite. In the analysis of engineering stability, linear Mohr–Coulomb and nonlinear Hoek–Brown criteria are generally considered as the yield criteria of rock masses. The basic parameters of the two models were still obtained from laboratory tests. When the Hoek–Brown criterion was adopted, the uniaxial compressive strength σ_c and rock hardness m of the complete rock samples were obtained from laboratory tests and the mechanical parameters of surrounding rocks were obtained by combining with the GSI surrounding rock rating system. When the Mohr–Coulomb criterion was adopted, the uniaxial compressive strength σ_c of intact rock and the peak and residual friction angles ϕ and cohesions c of the rock were determined. The fitting method proposed by Hoek and Brown [26] was applied for the calculation of peak and residual strength principal stress curves of the two criteria in this paper, as shown in Figure 6.

It can be seen from Figure 6 that high fitting accuracies were obtained for both Hoek–Brown strength curve and Mohr–11Coulomb intensity curve. The residual strength and peak value were obtained by the fitting method, as shown in Table 1. The Mohr–Coulomb strength parameters are easy to obtain, and the influence of rock dilatancy is considered in the practical engineering applications. Therefore, in this paper, the postpeak mechanical model of rock was investigated according to the Mohr–Coulomb strength criterion.

It can be seen from the analysis above that softening modulus coefficient ζ is the key to build a strain-softening model for rock. Optimal exponential fitting was performed in this work using the indoor triaxial compression test data. The equation of ζ under different confining pressures could be obtained as

$$\xi = -1.3e^{-0.072\sigma_3}. \tag{21}$$

Compared with other fitting equations, the exponential fitting method is more suitable for the secondary development and application of FLAC^{3D}. The average correlation coefficient of the fitting curve is more than 0.9, indicating that the nonlinear fitting effect of the model is remarkable. The fitting curve is shown in Figure 7.

4. Numerical Simulation of Local Fracture in Deep Granite

4.1. Numerical Model and Parameters. The local fracture characteristics of deep granite under strain-softening condition were evaluated using Mohr–Coulomb and Hoek–Brown strain-softening models. The model size was adopted to be 10 R, where $R = 2$ m to avoid boundary effects. The boundaries were normal fixed constraints. The initial ground stress was 25 MPa, and the lateral pressure coefficient was 1. Boundary conditions and calculation model are shown in Figure 8. In the process of numerical calculation, the strain-softening model of granite was written into the FLAC^{3D} strain-softening model by FISH language. The cohesion and internal friction angle were set as the bilinear function of the plastic parameter ε^{ps}, and the same plastic strain was experienced from the softening to residual stage. The nonlinear dilatancy angle of rock varied with the increase of plastic parameter ε^{ps}. After excavating the deep roadway surrounding rock, the virtual supporting pressure P_i was gradually reduced to realize the stress release process of the surrounding rock and analyze the evolution characteristics of the local rock local fracture. The calculation parameters of surrounding rock are shown in Table 1.

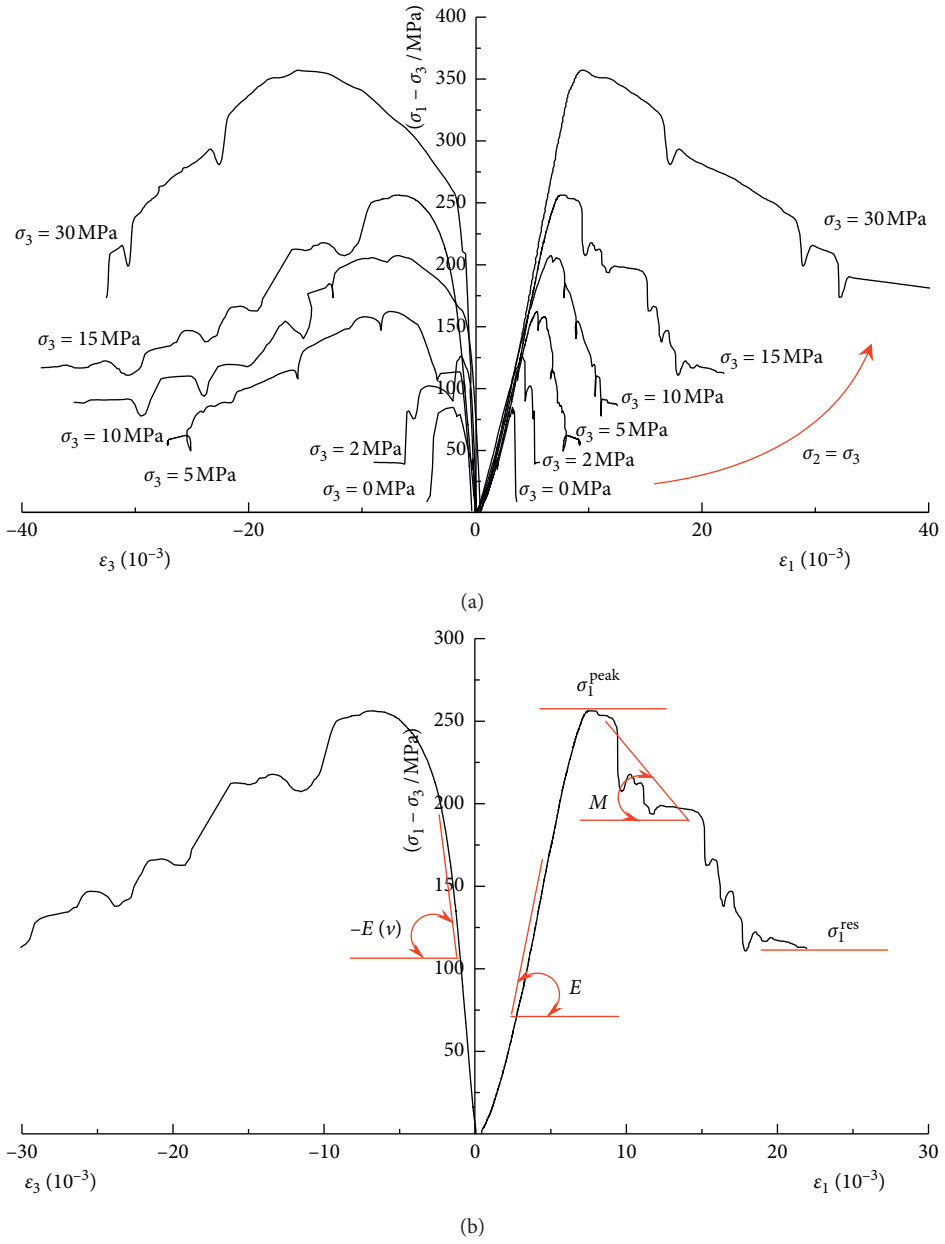

Figure 4: The complete stress-strain curves of granite. (a) Complete stress-strain curves of rock samples. (b) Complete stress-strain curves of rock samples with a confining pressure of 15 MPa.

(a) (b)

Figure 5: Characteristics of typical rock destruction. (a) Triaxial compression failure characteristics of granite samples. (b) Brazilian splitting fracture characteristics of granite samples.

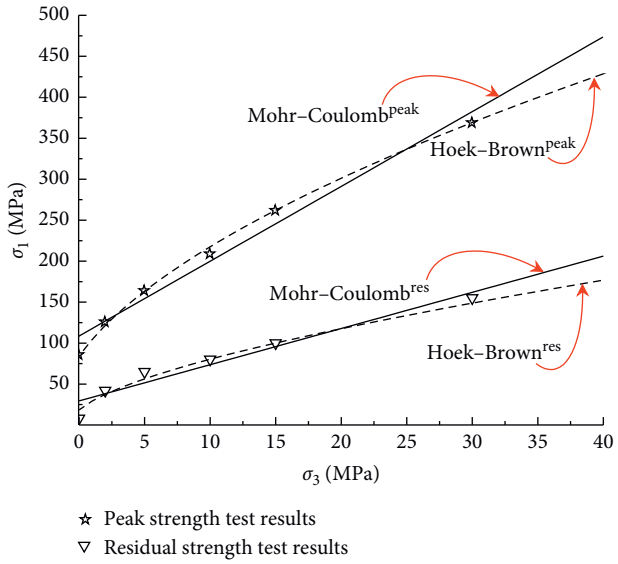

Figure 6: Granite strength fitted curves.

Table 1: Rock strength parameters.

Criterion	Hoek–Brown			Mohr–Coulomb				
Parameters	σ_c (MPa)	m	R^2	σ_c (MPa)	c (MPa)	Φ (°)	R^2	σ_t (MPa)
Peak	73.6	32	0.994	88.3	11.2	53.1	0.978	11.85
Residual	18.4	21	0.993	25.3	3.5	43.8	0.966	

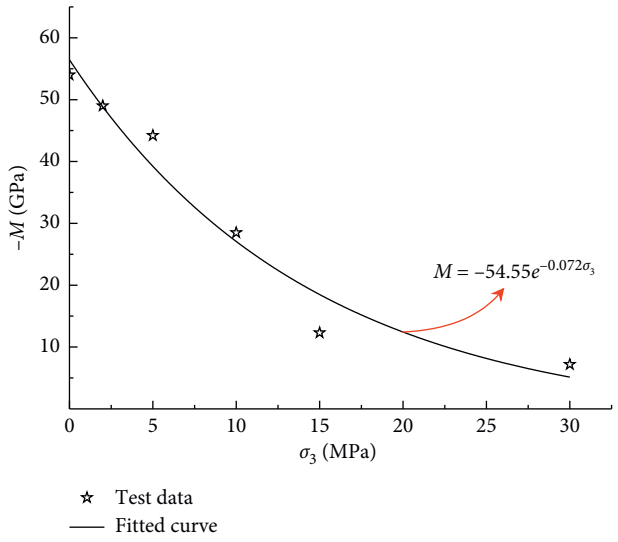

Figure 7: Softening modulus fitted curve after rock peak.

4.2. Local Fracture Characteristics of Granite. Calculations of the nonlinear dilatancy angle variation characteristics of the surrounding rock revealed that, with the continuous release of the surrounding rock stress, the dilatancy angle distribution moved from the surrounding rock surface to the deep layer, as shown in Figure 9. When the stress of the surrounding rock was released by 20%, the surface of the surrounding rock was the main area of capacity expansion.

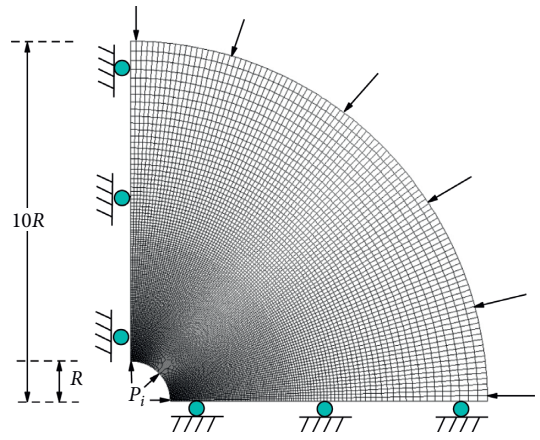

Figure 8: Calculation model and boundary conditions.

With the continued release of the stress of the surrounding rock, the dilatancy angle decreased and gradually shifted to the depth of the surrounding rock. It can be seen that the main capacity expansion phenomenon occurred in the surrounding rock near the working face with the excavation of the tunnel. When the working face continued to advance, the influence of the dilatancy angle on the surrounding rock surface gradually decreased and the dilatancy angle gradually decreased and moved to the deep rock mass. The nonlinear dilatancy angle was not concentrated in a certain area but changed with the increase of shear strain.

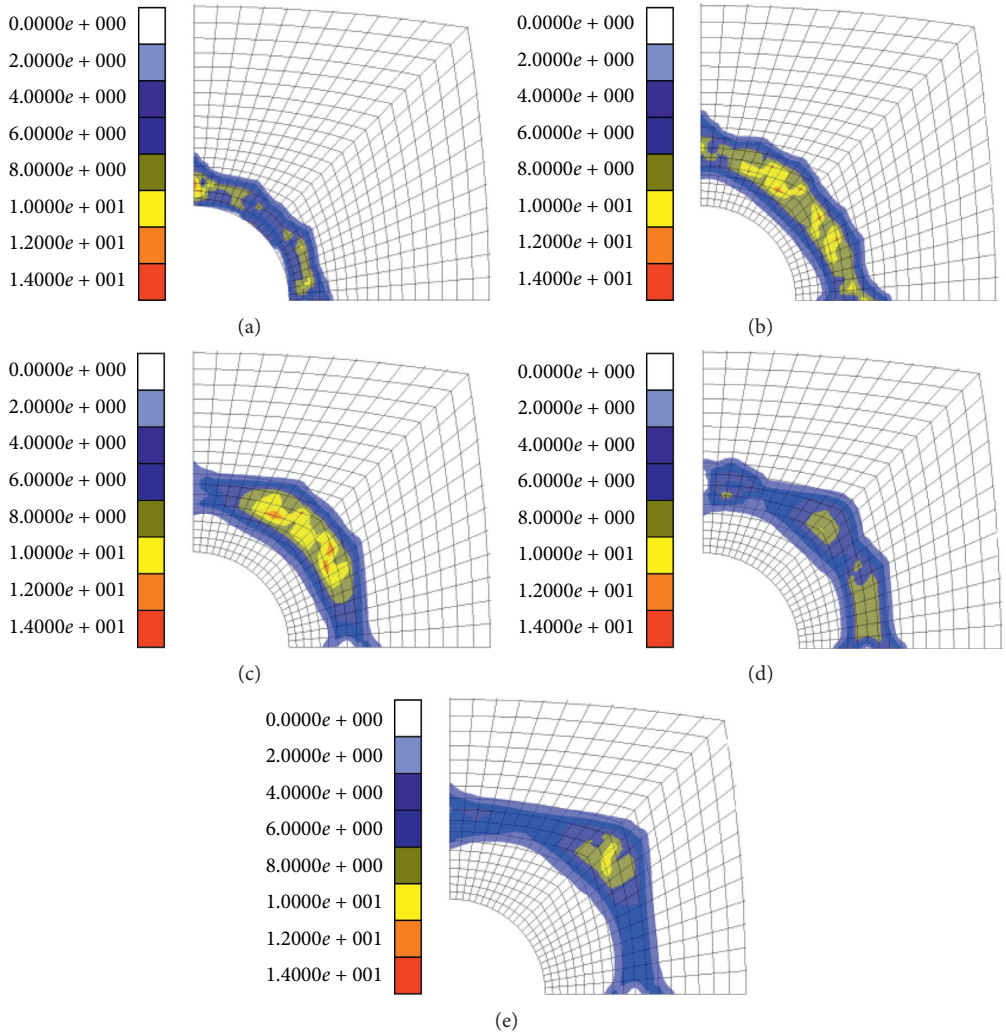

Figure 9: Variation of dilatancy angle of surrounding rock. (a) 20% released; (b) 40% released; (c) 60% released; (d) 80% released; (e) 100% released.

Calculations of the local fracture characteristics of surrounding rock revealed that the localized distribution ranges of the two yield criteria were relatively close, as shown in Figures 10(a) and 10(b). When the distortion of surrounding rock reached a threshold value, the inner wall section of the surrounding rock was first broken down and the rock entered residual strength stage. By further release of stress from surrounding rock, stress continued to expand into the surrounding rock. In addition, unbroken rock masses were distributed among banded spirals. Due to higher strain-softening parameters of granite, the ranges of stress bifurcation and strain localization generated by surrounding rocks were larger. The spiral fracture zone inside surrounding rock was very obvious. The main reason was that the strength of surrounding rock was decreased and its initial stress was high. During stress release, damage to surrounding rock was more serious such that the damage degree of surrounding rock surface in the cloud diagram of the Mohr–Coulomb model was more serious than that calculated by the Hoek–Brown model.

The bolt elements were installed when the load was released by 60% after surrounding rock excavation (length = 2.0 m, diameter = 18 mm, spacing = 1.2 m). By analyzing the local fracture characteristics of the surrounding rock under the condition of bolt support, it was known that the bolts had a controlling effect on the local fracture range of the surrounding rock. The calculation results are shown in Figures 10(c) and 10(d). The plastic strain rate of the bolts reinforcement zone decreased obviously, but the surrounding rock still showed the characteristics of local fracture. The calculated axial force distribution characteristics of bolts are shown in Figure 11. There was a certain difference in the axial force of bolts calculated by the two constitutive models. The main reason was that the Mohr–Coulomb model took into account the change of nonlinear dilatancy angle, which led to the increase of axial force of bolt. This was more in line with the actual situation of the project.

4.3. Analysis of Surrounding Rock Deformation Characteristic Curve. Many designers use numerical simulation methods

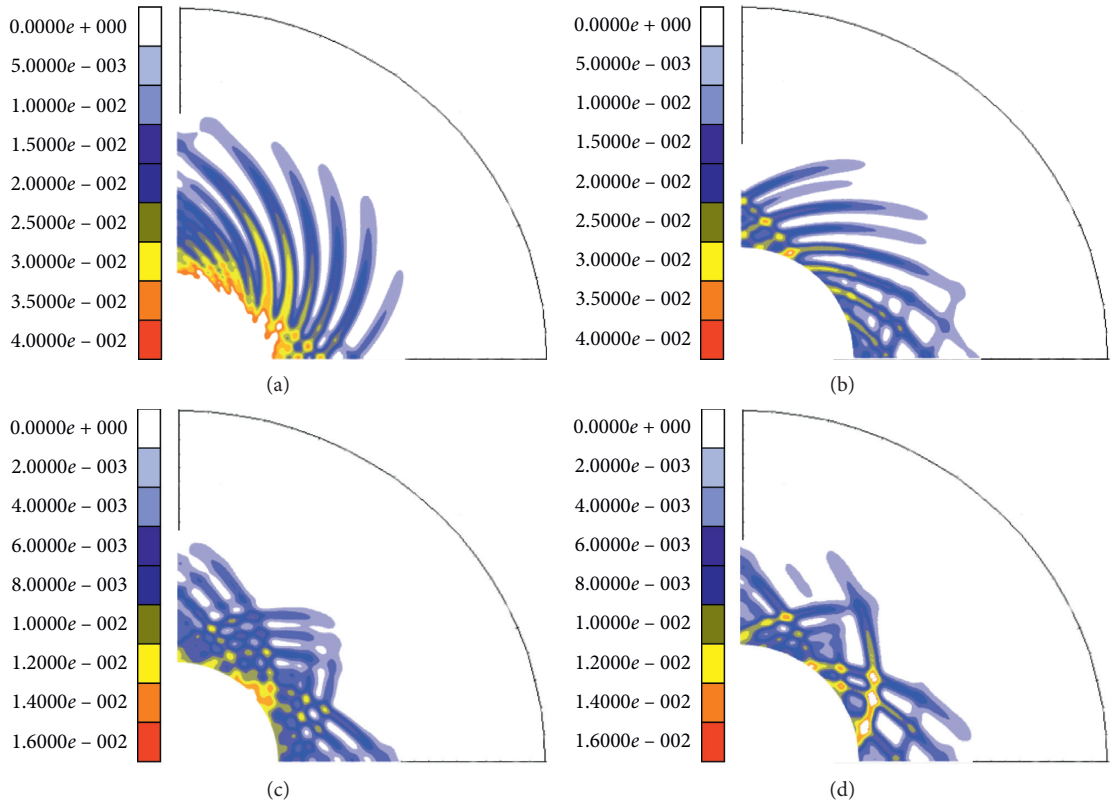

Figure 10: Distribution characteristics of regional fracture of surrounding rock. (a) M-C model; (b) H-B model; (c) M-C model bolt support; (d) H-B model bolt support.

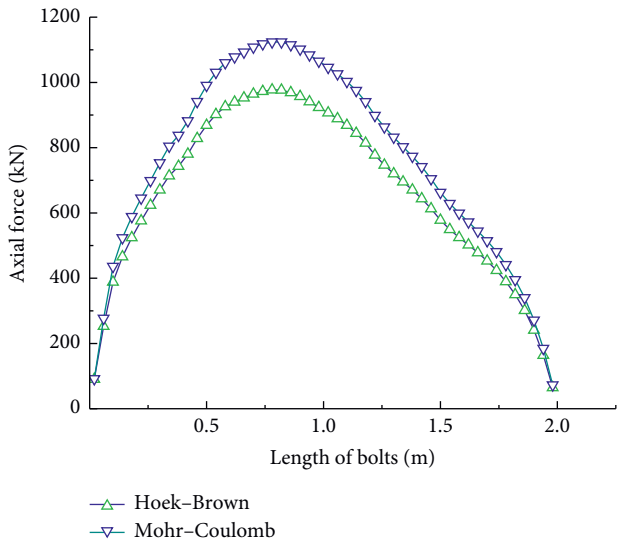

Figure 11: Axial force distribution of bolts.

for calculating the support structure of deep-buried roadways in engineering practices and usually establish rough numerical models. Numerical models with different grid densities were applied to investigate the effect of local cracking on the calculation of the stability of surrounding rock and supporting structure in this paper. The models are shown in Figure 12, where $R = 2$ m. The Mohr–Coulomb model and Hoek–Brown model were used in the calculation. It was assumed that the virtual internal support stress P_i of surrounding rocks was gradually decreased by 2% of the original rock stress each time, for 50 times in a cycle. Thus, the relation curve between the displacement and pressure of surrounding rock was obtained.

It can be seen from Figure 13 that the Hoek–Brown model and Mohr–Coulomb model were used to calculate the three different mesh accuracy models. The results showed that surrounding rock displacement in superfine model (a) was larger than that of the other two models, but the difference was small. It was seen that the obtained calculation accuracy met the requirements when calculating the stability of surrounding rocks and supporting the structures by numerical analysis methods, even when local cracking was not considered. However, the superfine mesh model could better study the distribution characteristics of local rupture and the interaction between supporting structure and surrounding rock, which could provide guidance for deep mining projects.

5. Study on the Local Fracture of Surrounding Rock in Deep Roadway

The design production level of Xincheng Gold Mine of Shandong Province in China is 1505 m (ground elevation + 50 m). Surrounding rocks in this section are mainly composed of granite with almost uniform and complete distribution of rock mass. The maximum horizontal ground

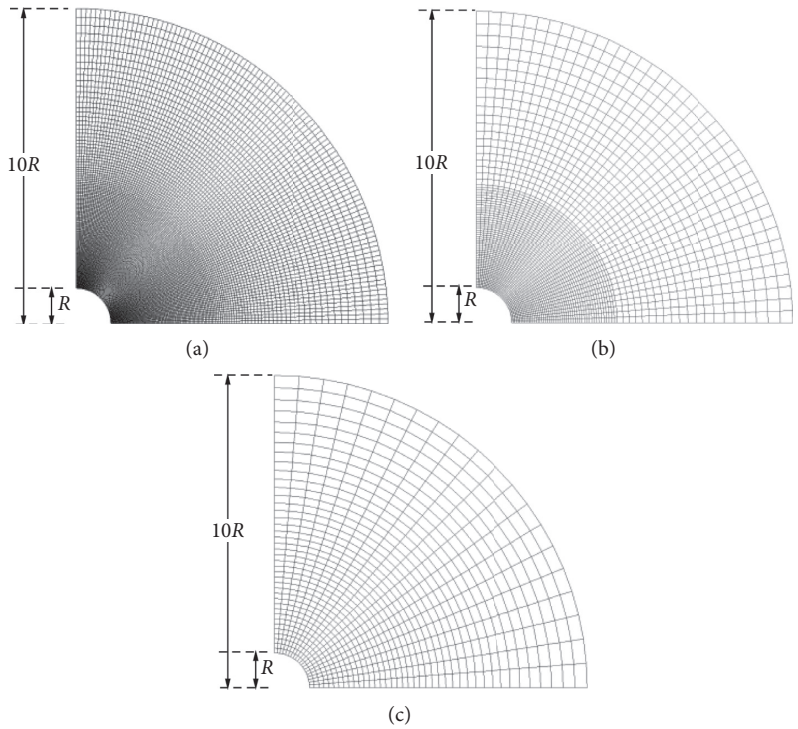

Figure 12: Numerical models with different grid densities. (a) High density. (c) Medium density. (d) Low density.

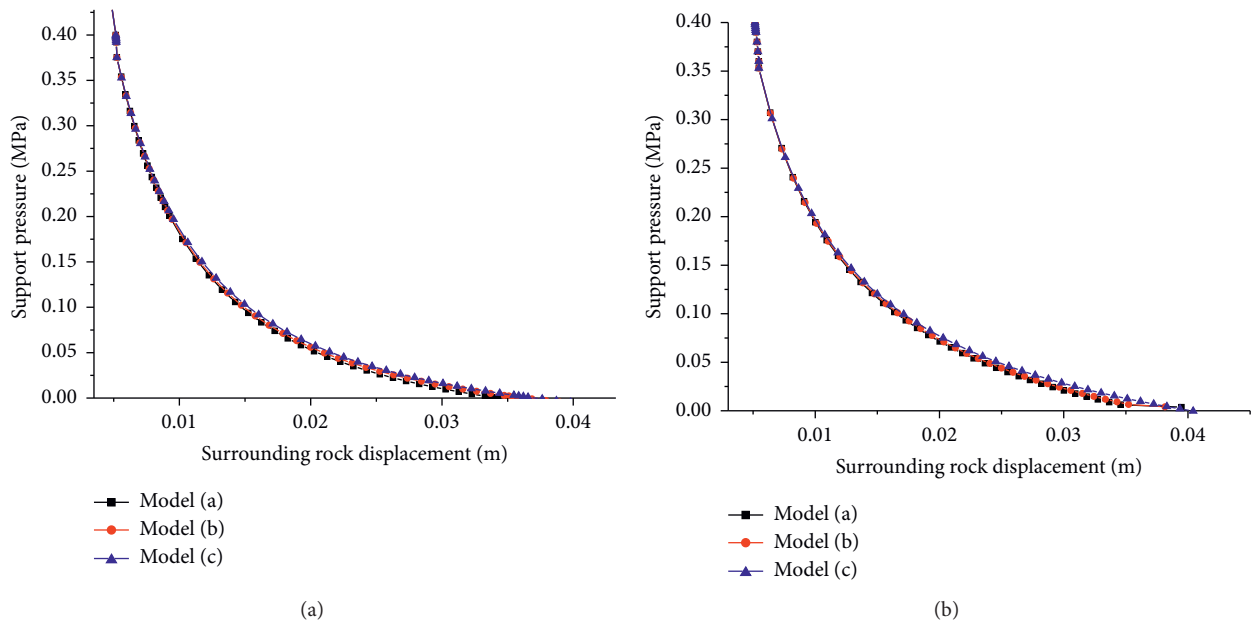

Figure 13: Deformation characteristics of surrounding rock. (a) Mohr–Coulomb model. (b) Hoek–Brown model.

stress value is 30 MPa, and the vertical ground stress value is 25 MPa. This is a high geostress environment. For accurate prediction of potential damage area of roadway surrounding rock, a two-dimensional fine numerical grid element model of roadway was developed in this paper. Based on the strain-softening model of granite, the location of post-peak failure area of deep surrounding rock was analyzed. The size and boundary conditions of the numerical model are shown in Figure 14, where horizontal ground stress value $P_x = 30$ MPa and vertical ground stress value $P_y = 25$ MPa. The surrounding rock parameters in calculation are shown in the Mohr–Coulomb strength parameters in Table 1.

According to calculations and analyses, under the action of high geostress, a large area of plastic shear failure area still appeared in roadway vault and arch foot although the lithology of roadway surrounding rocks was relatively hard, as shown in Figure 15. The damage area of roadway vault was still a low confining pressure area. Surrounding rock failure

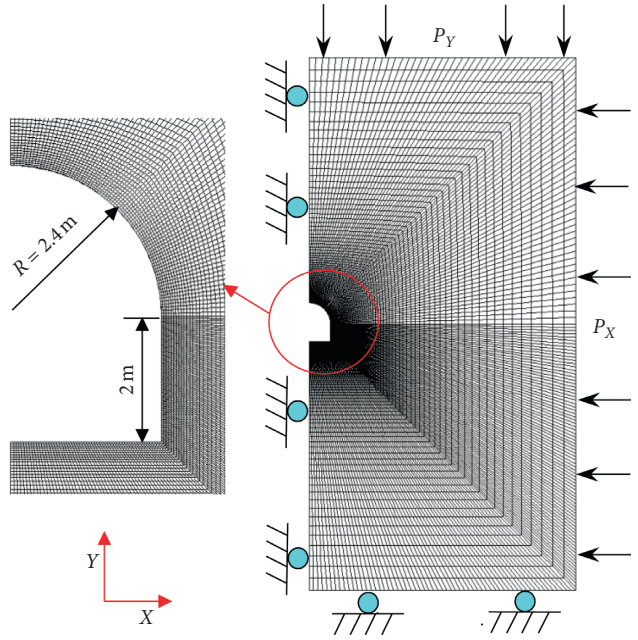

Figure 14: Numerical calculation model of the roadway.

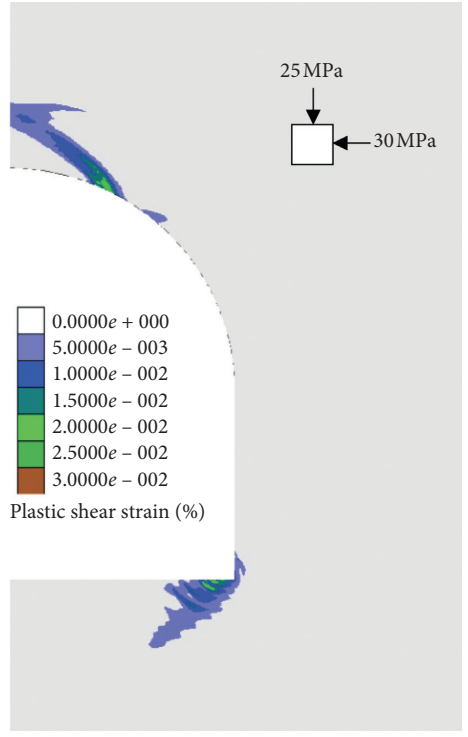

Figure 15: Diagram of surrounding rock shear plastic zone distribution.

mode was mainly brittle failure, and failure area did not extend to deep surrounding rocks. During actual construction and for a period of time after construction, some damage took place in vault surrounding rocks, as shown in Figure 16. Damage depth was basically the same as the calculation result. It can be seen that the granite strain-softening model developed in this work could reasonably reflect the postpeak failure characteristics of rocks, and calculation results could provide relevant suggestions for the construction site.

(a) (b)

Figure 16: Failure characteristics of the surrounding rock of the deep roadway. (a) Vault failure characteristics. (b) Rock mass characteristics of the side wall of the roadway.

6. Conclusion

Based on the deep mining project, a strain-softening model for granite was established in this work. The local fracture characteristics of deep granite were studied, and the obtained results were applied to engineering practice. The following conclusions are drawn:

(1) By analyzing the properties of triaxial complete stress-strain curves obtained for granite, it was found that the postpeak failure characteristics of granite obviously correlated with the confining pressure. The postpeak failure tended to brittle-ductile transformation. The increase of the confining pressure decreased the postpeak softening moduli of rocks, but it was not obvious under low and medium confining pressures. However, rocks still exhibited brittle failure characteristics after the strength of rock reached its peak value under high confining pressure conditions.

(2) Based on the theory of plastic mechanics, the functional relationship between postpeak softening modulus of granite and surrounding rock was obtained by the exponential fitting method. The strain-softening model of granite considering nonlinear dilatancy angle was deduced, and the model was solved by FLAC^{3D}. Calculations revealed that the deep granite had obvious local fracture characteristics, and the surrounding rock characteristic curves obtained by the numerical models with different grid densities were basically the same. The results showed that, when the convergence constraint method or numerical model was used to calculate the stability of surrounding rock and supporting structure, the local cracking phenomenon would have little influence on the calculation results.

(3) A wide plastic shear strain area was seen in the roadway vault and arch foot by numerical analyses on the failure characteristics of surrounding rocks in the deep granite roadway. It was basically the same location and depth of the surrounding rock failure of the onsite roadway. The postpeak strain-softening model of granite based on the Mohr–Coulomb model can take into account the change of dilatancy angle, which was more suitable for deep rock mass engineering.

Data Availability

The data used to support the findings of this study are available from the corresponding author upon request.

Conflicts of Interest

The authors declare that there are no conflicts of interest regarding the publication of this paper.

Acknowledgments

The authors would like to thank the support from the National Key R&D Projects (Grant no. 2017YFC1503101), National Natural Science Foundation of China (Grant no. 51704144), and Talent Project of Revitalizing Liaoning Funding Project (Grant no. XLYC1807107).

References

[1] X. Q. Zhou, J. Yu, J. B. Ye, S. Y. Liu, R. G. Liao, and X. W. Li, "Complex modeling of the effects of blasting on the stability of surrounding rocks and embankment in water-conveyance tunnels," *Complexity*, pp. 1–9, 2018.

[2] Y. K. Lee and S. Pietruszczak, "A new numerical procedure for elasto-plastic analysis of a circular opening excavated in a strain-softening rock mass," *Tunnelling and Underground Space Technology*, vol. 23, no. 5, pp. 588–599, 2008.

[3] L. R. Alejano, A. Rodríguez-Dono, and M. Veiga, "Plastic radii and longitudinal deformation profiles of tunnels excavated in strain-softening rock masses," *Tunnelling and Underground Space Technology*, vol. 30, no. 4, pp. 169–182, 2012.

[4] A. Manouchehrian and M. Cai, "Influence of material heterogeneity on failure intensity in unstable rock failure," *Computers and Geotechnics*, vol. 71, pp. 237–246, 2016.

[5] V. Hajiabdolmajid, P. K. Kaiser, and C. D. Martin, "Modelling brittle failure of rock," *International Journal of Rock Mechanics and Mining Sciences*, vol. 39, no. 6, pp. 731–741, 2002.

[6] C. Sun, X. D. Zhang, and Y. J. Li, "Soft rock equivalent mechanical model of post-peak in deep and numerical computing research," *Chinese Journal of Geotechnical Engineering*, vol. 36, no. 6, pp. 1113–1122, 2014, in Chinese.

[7] J. Ma, P. Yin, L. Huang, and Y. Liang, "The application of distinct lattice spring model to zonal disintegration within deep rock masses," *Tunnelling and Underground Space Technology*, vol. 90, no. 8, pp. 144–161, 2019.

[8] V. V. Makarov, M. A. Guzev, V. N. Odintsev, and L. S. Ksendzenko, "Periodical zonal character of damage near the openings in highly-stressed rock mass conditions," *Journal of Rock Mechanics and Geotechnical Engineering*, vol. 8, no. 2, pp. 164–169, 2016.

[9] J. Bi and X. P. Zhou, "Numerical simulation of zonal disintegration of the surrounding rock masses around a deep circular tunnel under dynamic unloading," *International Journal of Computational Methods*, vol. 12, no. 03, Article ID 1550020, 2015.

[10] F. Varas, E. Alonso, L. R. Alejano, and G. Fdez-Manín, "Study of bifurcation in the problem of unloading a circular excavation in a strain-softening material," *Tunnelling and Underground Space Technology*, vol. 20, no. 4, pp. 311–322, 2004.

[11] P. Egger, "Design and construction aspects of deep tunnels (with particular emphasis on strain softening rocks)," *Tunnelling and Underground Space Technology*, vol. 15, no. 4, pp. 403–408, 2000.

[12] S. C. Li, X. D. Feng, C. Yuan, W. Li, and Q. Sun, "Numerical simulation of zonal disintegration for deep rock mass," *Chinese Journal of Rock Mechanics and Engineering*, vol. 30, no. 7, pp. 1337–1344, 2011.

[13] I. Pérez-Rey, L. R. Alejano, E. Alonso, J. Arzúa, and M. Araújo, "An assessment of the post-peak strain behavior of laboratory intact rock specimens based on different dilation models," *Procedia Engineering*, vol. 191, pp. 394–401, 2017.

[14] Y. L. Lu, L. G. Wang, F. Yang, Y. Li, and H. Chen, "Post-peak strain softening mechanical properties of weak rock," *Chinese Journal of Rock Mechanics and Engineering*, vol. 29, no. 3, pp. 640–649, 2010, in Chinese.

[15] H. Z. Yu, H. N. Ruan, and W. J. Chu, "Mesoscopic simulation study of brittle-ductile-plastic transition character of marble," *Chinese Journal of Rock Mechanics and Engineering*, vol. 32, no. 1, pp. 55–65, 2013, in Chinese.

[16] J. Yu, G. Y. Liu, Y. Y. Cai, J. F. Zhou, S. Y. Liu, and B. X. Tu, "Time-dependent deformation mechanism for swelling soft-rock tunnels in coal mines and its mathematical deduction," *International Journal of Geomechanics*, vol. 20, no. 3, Article ID 04019186, 2020.

[17] M. R. Zareifard, "Ground response curve of deep circular tunnel in rock mass exhibiting Hoek-Brown strain-softening behaviour considering the dead weight loading," *European Journal of Environmental and Civil Engineering*, pp. 1–31, 2019.

[18] L. R. Alejano, A. Rodriguez-Dono, E. Alonso, and G. Fdez-Manín, "Ground reaction curves for tunnels excavated in different quality rock masses showing several types of post-failure behaviour," *Tunnelling and Underground Space Technology*, vol. 24, no. 6, pp. 689–705, 2009.

[19] L. R. Alejano, A. Rodriguez-Dono, E. Alonso, and G. F. Manín, "Application of the convergence confinement method to tunnels in rock masses exhibiting hoek-brown strain-softening behaviour," *International Journal of Rock Mechanics and Mining Sciences*, vol. 47, no. 1, pp. 150–160, 2010.

[20] S. K. Sharan, "Analytical solutions for stresses and displacements around a circular opening in a generalized hoek-brown rock," *International Journal of Rock Mechanics and Mining Sciences*, vol. 45, no. 1, pp. 78–85, 2008.

[21] A. Ghorban and H. Hasanzadehshooiili, "A comprehensive solution for the calculation of ground reaction curve in the crown and sidewalls of circular tunnels in the elastic-plastic-EDZ rock mass considering strain softening," *Tunnelling and Underground Space Technology*, vol. 84, pp. 413–431, 2019.

[22] S. L. Wang, Z. J. Wu, C. G. Li, and H. Tang, "Modeling of strain-softening and analysis of a lining for circular tunnel," *Rock and Soil Mechanics*, vol. 31, no. 6, pp. 1929–1937, 2010, in Chinese.

[23] Q. Zhang, H.-Y. Wang, Y.-J. Jiang, M.-M. Lu, and B.-S. Jiang, "A numerical large strain solution for circular tunnels excavated in strain-softening rock masses," *Computers and Geotechnics*, vol. 114, Article ID 103142, 2019.

[24] C. Sun, X. D. Zhang, and Y. J. Li, "Analysis of interaction between surrounding rock and support under high stressed soft rock roadway," *Rock and Soil Mechanics*, vol. 34, no. 9, pp. 2601–2609, 2013, in Chinese.

[25] J. Arzu and L. R. Alejano, "Dilation in granite during servo-controlled triaxial strength tests," *International Journal of Rock Mechanics and Mining Sciences*, vol. 61, no. 3, pp. 43–56, 2013.

[26] E. Hoek and E. T. Brown, "Practical estimates of rock mass strength," *International Journal of Rock Mechanics and Mining Sciences*, vol. 34, no. 8, pp. 1165–1186, 1997.

[27] X. G. Zhao and M. Cai, "A mobilized dilation angle model for rocks," *International Journal of Rock Mechanics and Mining Sciences*, vol. 47, no. 3, pp. 368–384, 2010.